Multidirectional porous NiO nanoplatelet-like mosaics as catalysts for green chemical transformations

Sherif A. El-Safty [a,b,*], Mohamed Khairy [a,b], Mohamd. Ismael [a], Hiroshi Kawarada [b]

[a] National Institute for Materials Science (NIMS), 1-2-1 Sengen, Tsukuba-shi, Ibaraki-ken 305-0047, Japan
[b] Graduate School for Advanced Science and Engineering, Waseda University, 3-4-1 Okubo, Shinjuku-ku, Tokyo 169-8555, Japan

ABSTRACT

The design of multidirectional porous metal oxide catalysts has attracted extensive attention because such materials have potential for environmental applications. To satisfy the requirements of these applications, large-scale production, low-cost manufacturing, and efficient transformation reactions are needed. The present paper reports the fabrication of hierarchical nickel oxide nanocrystals (NiO NCs) with hexagonal nanoplatelets and micro-, meso-, and macropore cavities through an eco-friendly method. The controlled size and shape of the NiO platelets in condensed orientation sequence "tesserae blocks" led to the formation of a hexagonal mosaic-like morphology. The NiO NCs could be recovered and reused without lost of activity over a number of batch reactions. In addition, theoretical models to predict the molecular structures of both the intermediate and transition states within the chemical transformation reactions were developed. The theoretical findings in the current study provide insight into the key factors that control the changes in the molecular structure throughout the transformation mechanism of the phenolic pollutants using NiO platelet nanocatalysts.

© 2012 Elsevier B.V. All rights reserved.

1. Introduction

In recent years, hierarchically structured porous metal oxide nanostructures have received extensive attention in the field of research because of their large surface areas, hydrothermal stability in organic and inorganic solution phases, and reduced densities, as well as unique optical, electronic, and magnetic features that lead to a broad range of applications in sensors [1,2], optical imaging [3], phototherapy [4], catalysis [5,6], nanofiltration [7,8], and energy generation [9,10]. Efforts have been directed toward the synthesis of porous metal oxide nanostructures, aiming to control the intrinsic structure and morphology of these materials for tunable properties. However, technical challenges in terms of intensive and time-consuming synthetic conditions remain. Template synthetic methods have been established as convenient approaches to synthesize porous metal oxides. In these methods, either organic or inorganic particles are used as sacrificial templates. However, during the removal of these templates at high temperature, the mesoporous structures tend to collapse. Furthermore, the

formation of amorphous and/or semi-crystalline walls using these metal oxide nanostructures could restrain their practical utility [11].

Nickel oxide nanocrystals (NiO NCs), with uniform morphologies and sizes, are potential candidates for a variety of applications in catalysis, electrochronic display devices, optical gas sensors, antiferromagnetic layers, dye-sensitized photo-cathodes, lithium ion batteries, and solar thermal absorbers [12–16]. Gedanken et al. [17] reported a sonochemical method for synthesizing nickel hydroxide $(Ni(OH)_2)$ clusters. Chaudre et al. [18] reported the fabrication of nickel nanorods with the possibility of tuning their sizes and, therefore, their magnetic properties. High-order mesoporous NiO was prepared via a nanocasting technique using a cubic mesostructured silica KIT-6 as the solid template. Given the large surface area, shorter pathway for diffusion, and lower activation energy of mesoporous NiO, enhanced electrochemical responses of these nanostructures were observed [19]. Nanosized NiO crystals with uniform morphologies have been successfully fabricated using reliable methods [20,21]. However, controlling the formation and arrangement of the nanoplatelets in the mosaic structure with multidirectional micro-, meso-, and macroporous NiO crystals during their growth and nucleation may lead to promising applications. Hu et al. [22] reported the formation of crystalline NiO [1 1 1] nano-sheets with holes through wet chemical synthesis. However, the process required intensive and complicated synthetic strategies that involved high pressure, salt–solvent mediators, high temperature, structure-directing agents, or organometallic precursors.

* Corresponding author at: National Institute for Materials Science (NIMS), 1-2-1 Sengen, Tsukuba-shi, Ibaraki-ken 305-0047, Japan/Graduate School for Advanced Science and Engineering, Waseda University, 3-4-1 Okubo, Shinjuku-ku, Tokyo 169-8555, Japan. Tel.: +81 29 859 2135.
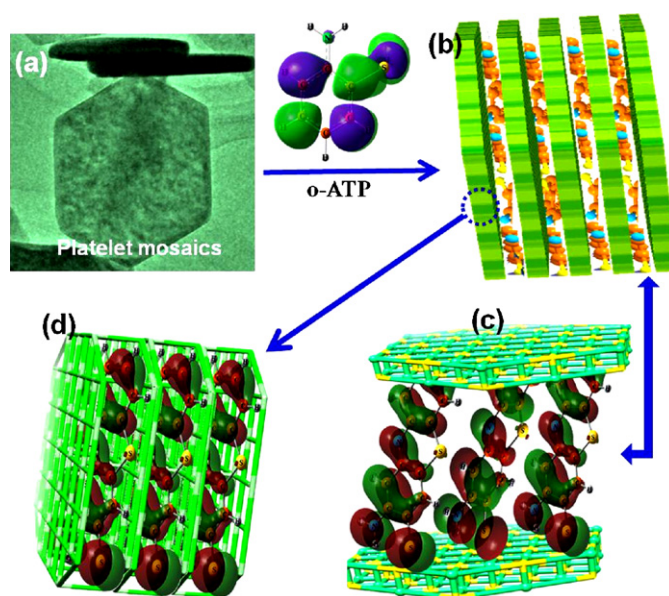*E-mail addresses:* sherif.elsafty@nims.go.jp, sherif@aoni.waseda.jp (S.A. El-Safty).

Thus, a design of a simple method for the size-controlled morphology, multidirectional porosity, and NC structure of NiO is highly desirable.

Environmental problems, such as organic and toxic water pollutants, provide the impetus for fundamental and applied research in catalytic processes for detoxifying the pollutants. Such challenges result in the need for greener chemical products and the transformation of hazardous chemicals [23]. In addition, petrochemical, chemical, and pharmaceutical industries produce wastewater containing high concentrations of organic materials, which may be difficult to oxidize biologically and are extremely toxic to aquatic life [24]. Considering the increasing concern for public health and environmental quality, the complete removal of organic pollutants from the environment, particularly wastewater, is imperative and presents a great challenge to water suppliers [25]. Recently, different strategies to remove organic pollutants from aqueous water, including adsorption [26,27], ion exchange [28], membrane filtration [7,8,29], and chemical oxidation [30] have been used. A more efficient and cost-effective method of removing organic pollutants from water is needed. The chemical transformation or chemical oxidation of these pollutants is one of the most commonly adopted methods in refinery techniques to produce safe compounds. Phenolic compounds, such as aminophenols (APs), have a variety of uses as reducing agents, intermediates in chemical synthesis, bleaching and hair dyes, and materials for photography. In addition, APs are highly important in producing phenoxazone compounds, including questiomycin A, which is related to the natural antineoplastic agent actinomycin D. The latter is used clinically for the treatment of certain types of cancer [31]. APs are one of the most common organic pollutants, and their toxicity depends on relative position of the amino and hydroxyl groups, in which the toxicity of o-aminophenols (o-AP) is stronger than that of m-aminophenols (m-AP) and p-aminophenols (p-AP) [32]. According to the Natural Skincare Authority report, o-AP is a suspected teratogen, which has immunotoxicity, endocrine toxicity, and skin or sense organ toxicity. Meanwhile, o-aminothiophenol (o-ATP) is used as an antinematodal agent and converts oxyhemoglobin to methemoglobin; it is also used in the study of toxicity levels in human red blood cells [33].

Porous NiO NPs with high surface area and surface characteristics can act as effective catalysts in many chemical transformation processes [34]. Recently, mesoporous NiO nanosheets were fabricated through direct hydrothermal synthesis [35]. These NiO nanosheets show potential in gas sensing responses of low-level NO_2 concentrations. However, the practical design of nanocatalysts requires controlled assessment processes, which involve high-performance molecular transport and adsorption of pollutant molecules into the pore networks. Hence, the preparation of multidirectional micro-, meso-, and macropore cavities of NiO-based catalysts that are simple, easy to use, and have appropriate dynamic working ranges still remains a challenge.

In the present study, a simple and reproducible fabrication method of hierarchical NiO NCs with hexagonal nanoplatelets and micro-, meso-, and macropore cavities is reported. The proposed approach shows evidence of controlled size and shape of hexagonal NiO platelets in condensed orientation sequence "tesserae blocks," leading to the formation of a mosaic-like morphology. The mosaic features of NiO NCs induce high catalytic activity that enables the chemical transformation of phenolic pollutants into safe substances (Scheme 1). NiO platelet mosaic catalysts significantly offer highly stable catalytic activity even after several reuse cycles. To understand the proposed chemical transformation mechanism of pollutants, the energy profiles and the charge distribution of the reactants, intermediates, transition states, and products were calculated through the density function theory (DFT) method.

Scheme 1. Schematic of the chemical transformation of o-aminothiophenol over the NiO nanoplatelet-like mosaics; (a) HRTEM micrograph of NiO NCs with platelet-like morphology; (b) o-ATP molecules penetrating the nanoplatelet; (c) formation of 3-aminophenothiozine-3-thizone between platelets; (d) formation of 3-aminophenothiozine-3-thizone inside the pores of the platelets.

2. Experimental

2.1. Reagents

All materials were of analytical grade and used without further purification. Anhydrous nickel chloride, ammonium hydroxide, o-AP, EG, and o-ATP were purchased from Japan Tokyo Chemical Industry Company Ltd. (Japan). o-AP and o-ATP solutions ($0.015\,mol\,L^{-1}$) were prepared in water with 3% ethanol content at a phenol concentration of $5 \times 10^{-4}\,mol\,L^{-1}$ during the oxidation process.

2.2. General method for the fabrication of NiO nanoplatelet mosaic catalysts

Multidirectional micro-, meso-, and macropore NiO platelet mosaic catalysts were fabricated via a one pot and eco-friendly method (see Supplementary S1, Scheme S1). In a typical procedure, 2.58 g anhydrous nickel chloride was dissolved in 60 mL of distilled water and 20 mL of ethylene glycol (EG). The pH of the solution was adjusted to 10 via drop-wise addition of ammonia solution (28%). Then, the solution was loaded into the Teflon liner of a stainless steel autoclave with a volume of 100 mL. The autoclave was sealed and maintained at 160 °C for 6 h, and then the solution was allowed to cool to room temperature. Finally, the precipitate was obtained and washed several times with distilled water and ethanol to remove remaining agents. The precipitate collected by filtration, dried at 45 °C overnight and carefully calcined in air by heating at 2 °C/min from room temperature up to 300 °C. The product was maintained for 2 h to obtain the NiO nanoplatelet-like morphology. The porous NiO nanocatalyst was formed through the thermal decomposition of Ni(OH)$_2$ [Fig. S2]. The generation of mesopores within the NiO nanoplatelet samples was attributed to the dehydroxylation of Ni(OH)$_2$ and growth of NiO NCs at high-temperature treatments without changes in the nanoplatelet morphology.

2.3. Batch chemical transformation method of organic pollutants

The catalytic transformation of phenolic compounds was performed using NiO nanoplatelets as catalysts. The stock solution of phenolic compounds was prepared in water/3% ethanol (v/v) mixture. However the percentage of ethanol is less than 0.15% in reaction vessel. The heterogeneous catalytic reaction was performed at various temperature ranges within 25–40 °C using a thermostated shaker at a constant shaking rate. In a typical kinetic experiment, the catalyst (0.83 g/L) was mixed with 28 mL of deionized water purged with N_2 gas in closed Erlenmeyer-flask. The content was placed in a water shaker thermostat for 10 min at a specific temperature. A standard solution of phenol (2 mL) was added to the mixture with a micropipette and then the time was recorded. The concentration of phenols was 0.5 mM in the reaction vessel. After a set interval of time, an aliquot volume (3 mL) was transferred into the quartz cell to quench the reaction. No filtration or centrifugation system was used for detection of the reaction over NiO nanocatalyst, indicating easy batch contact-time experiments. The heterogeneous catalytic reaction was monitored spectrophotometrically at 435 and 322 nm for 3-APZ and 3-APT, respectively. To reuse the NiO catalyst after the first set of reaction experiments, the solid catalyst was collected and washed by 0.01 M HCl solution for several times and then dried at 200 °C overnight under air to remove the adsorbate product into interior/exterior pore surfaces.

Modeling calculations of the cyclization of 3-APZ and 3-APT products were done based on DFT calculations implemented in the Gaussian 03 suite program [36]. All calculations performed using an ordinary B3LYP functional theory, which comprises the hybrid Becke + Hartree–Fock exchange and Lee–Yang–Parr functional correlation with nonlocal corrections, were adopted with the basis set to 6-311++G (d, p). The solvent effects on the models were achieved using the polarized continuum model to obtain more reliable data.

2.4. Characterization of NiO nanocatalysts

The morphologies of the as-synthesized and calcined Ni samples were investigated by field emission scanning electron microscopy (FESEM, JEOL model 6500). Before insertion into the chamber, the NiO powders were grinded and fixed to a specimen stub using a double-sided carbon tape. Then, a 10 nm Pt film was coated by anion sputtering (HitachiE-1030) at room temperature to obtain high-resolution micrographs. Before sputtering deposition, the Pt target (4 in diameter, purity 99.95%) was sputter cleaned in pure Ar. The sputtering deposition system used for the experiments consists of a stainless steel chamber, evacuated down to 8×10^{-5} Pa with a turbo molecular pump backed up by a rotary pump. The Ar working pressure (2.8×10^{-1} Pa), the power supply (100 W) and the deposition rate were kept constant throughout these investigations. Moreover, to better record the SEM images of the Ni samples, the scanning electron microscope was operated at 20 keV. High-resolution transmission electron microscopy (HRTEM), electron diffraction (ED), scanning transmission electron microscopy (STEM), and energy dispersive X-ray spectroscopy for elemental mapping (STEM-EDS) were performed using a JEOL JEM model 2100F microscope. HRTEM was conducted at an acceleration voltage of 200 kV to obtain a lattice resolution of 0.1 nm. The HRTEM images were recorded using a CCD camera. STEM and STEM-EDS were carried out at a camera length of 80 cm and a spot size of 1 nm. In the HRTEM, ED, STEM, and STEM-EDS characterization, the NiO sample was dispersed in ethanol solution using an ultrasonic cleaner, and then dropped on a copper grid. Prior to inserting the samples in the HRTEM column, the grid was vacuum dried for 20 min.

Small angle X-ray scattering (SAXS) experiments were performed at room temperature. A two-dimensional (2D) confocal mirror (Rigaku Nanoviewer) and a pinhole collimator were used to obtain a focused high flux/high transmission; a monochromatic X-ray beam of Cu Kα radiation ($\lambda = 1.54$ Å) was also used. The 2D SAXS patterns were recorded using a 2D detector (BrukerHi-Star) covering a range of momentum transfer $q = (4\pi/\lambda) \sin(2\theta/2)$, from 0.2 to 10 cm^{-1}, where λ is the wavelength of the incident X-ray beam and 2θ is the scattering angle. The value of inter-particle distance (center to center) was calculated from $d = 2\pi/q_{max}$. Wide angle powder X-ray diffraction (XRD) patterns were measured using an 18 kW diffractometer (Bruker D8 Advance) with monochromated Cu Kα radiation. The sample measurement was repeated three times under rotation at various angles (15°, 30°, and 45°). The diffraction data were analyzed using the DIFRAC plus Evaluation Package (EVA) software with PDF-2 Release 2009 databases provided by Bruker AXS. The standard diffraction data were identified according to the databases of the International Centre for Diffraction Data (ICDD). For poor quality diffraction data, the TOPAS package program provided by Bruker AXS 2009 for profile and structure analysis was applied to integrate various types of X-ray diffraction analyses by supporting all profile fit methods currently employed in powder diffractometry.

The textural surface properties and pore size distribution were determined by N_2 adsorption/desorption isotherms at 77 K with a BELSORP36 analyzer (JP. BEL Co., Ltd.). Prior to the adsorption/desorption process, all the samples were pre-treated at 200 °C for 4 h under vacuum until the pressure was equilibrated to 10^{-3} Torr. The specific surface area (S_{BET}) was calculated using the Brunauer–Emmett–Teller (BET) method with multipoint adsorption data from the linear segment of the N_2 adsorption isotherm. The pore size distribution was determined using nonlocal density functional theory (NLDFT).

X-ray photoelectron spectroscopy (XPS) was conducted using a PHI Quantera SXM (ULVAC-PHI) (Perkin–Elmer Co., USA) with monochromated Al Kα radiation (1.5×0.1 mm, 15 kV, 50 W). Thermogravimetric and differential thermal analyses (TG and DTA, respectively) were measured using a simultaneous DTA-TG Apparatus TG-60 (Shimadzu, Japan). The absorbance spectrum of the heterogeneous catalytic reactions was recorded using a UV-Vis spectrophotometer (Shimadzu 3150, Japan).

3. Results and discussion

3.1. Formation of porous NiO nanoplatelet catalysts

The possible mechanism behind the formation of the NiO nanoplatelets (see Scheme S1) involved three stages: nucleation, growth, and dehydroxylation. Nucleation, that is, the precipitation of Ni^{2+} in pH 10 as $Ni(OH)_2$, proceeded too rapidly to generate nuclei. Second, the $Ni(OH)_2$ nanoplatelets were formed via a hydrothermal technique. The addition of EG to the synthesized composition was key to the controlled hexagonal morphology with dense and condensed orientation during the growth of the NCs. The controlled size and shape of the hexagonal NiO platelets in the condensed orientation sequence "tesserae blocks" significantly led to the formation of mosaic-like structures. Third, the dehydroxylation of $Ni(OH)_2$ under mild thermal treatment led to the generation of micro-, meso-, macroporous NiO with hexagonal platelet-like mosaics. The thermal decomposition of $Ni(OH)_2$ moieties was studied using thermogravimetry-differential thermal analysis (TG-DTA) techniques. The TG profile (Fig. S2) revealed the decrease in the mass of $Ni(OH)_2$ decreased at around 270–340 °C. This decrease was accompanied by an endothermic peak in the corresponding DTA curve, indicating the dehydroxylation of $Ni(OH)_2$. The weight loss from the decomposition of $Ni(OH)_2$ was 17.45 wt%, which is consistent with that in previous reports [37].
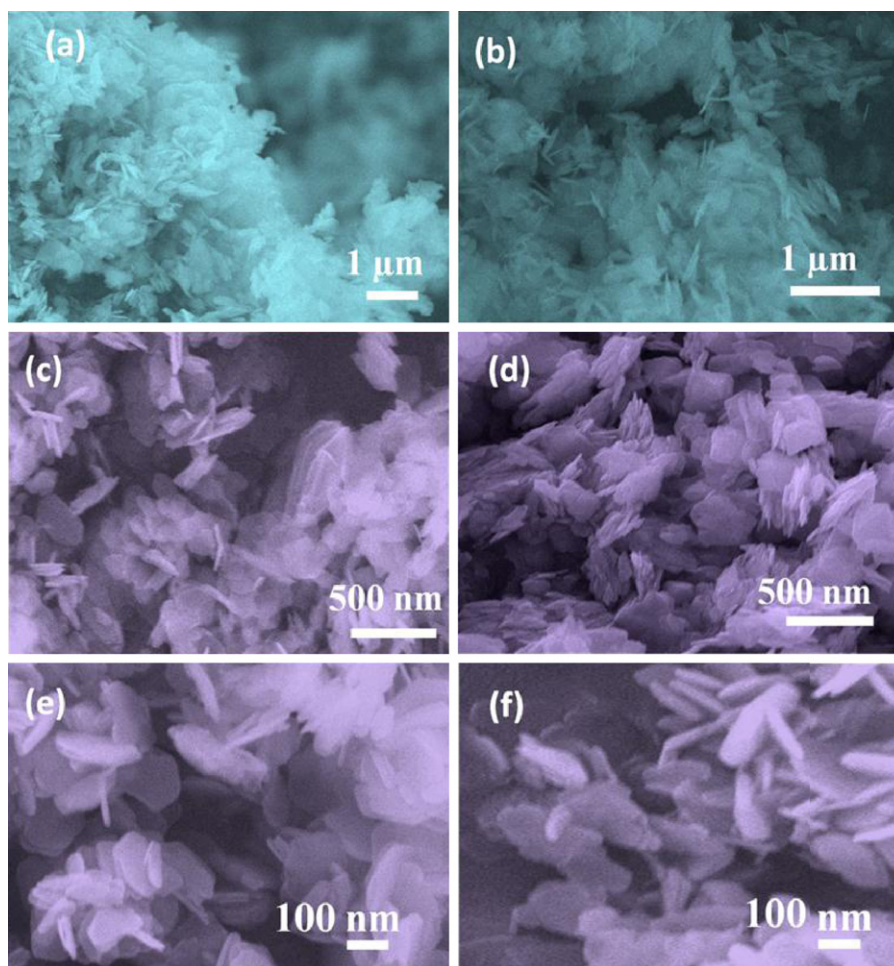
Fig. 1. FE-SEM micrograph of the NiO nanocatalyst: (a and b) β-Ni(OH)$_2$ phase and (c–f) calcined products of hexagonal NiO nanoplatelets.

3.2. Design of multidirectional micro-, meso-, and macroporous NiO nanoplatelet mosaic catalysts

Control over the particle morphology of Ni(OH)$_2$ and NiO was evident (Fig. 1). Field emission-scanning electron microscopy (FE-SEM) micrographs revealed that Ni(OH)$_2$ and NiO had nanosized tesserae block (mosaics) particles with an average diameter of 150–250 nm and a thickness of about 20 nm. These mosaic particles were arranged in hexagonal platelets with smooth fine surfaces, according to the conditions of the synthesis. Furthermore, these results (Fig. 1c–e) indicated the retention of hexagonal nanoplatelets during the formation of NiO under temperature treatment at 300 °C. SEM images showed significant evidence of shape- and size-controlled NiO platelets in condensed orientation sequences, indicating the versatility of this method over the real control of the NiO mosaic geometry (Fig. 1c and d).

High-resolution transmission electron microscopy (HRTEM) images of the NiO samples clearly revealed the formation of regular and condensed hexagonal platelet mosaics with an average size of 250 nm (Fig. 2a–d). The nanoplatelets were very thin; the thickness was less than 20 nm, as shown in Fig. 2(b). In addition, the adjacent edge angle was approximately 120°, as shown in Fig. 2(b). The local structure of the nanoplatelets showed variable sizes of hexagonal morphology, indicating the formation of mosaic networks, despite the symmetric deviation with inter-planar angles from 60°. TEM micrographs (Fig. 2a–d) showed the formation of disordered (wormlike) mesopores (around 3.5 nm), based on scanning transmission electron microscopy (STEM), small angle X-ray scattering

(SAXS), and N$_2$ isothermal profiles (Figs. 3–6). The representative electron diffraction (ED) image (Fig. 2e) showed well-defined orientations of bright-dot incidences, indicating the formation of large-scale NC domains. The distance between two lattice fringes was 0.24 nm (Fig. 2e), which is consistent with the interplanar space of the (1 1 1) plane of the cubic NiO symmetry (Fig. 2f). Enlarged HRTEM images of selected areas (Fig. 2g and h) showed further evidence of the formation of a cubic Fm3m NiO NCs. The images revealed well-organized lattice arrays over a large area with distances of 0.2 nm and 0.149 nm, respectively, which feature the *d*-spacings of the (2 0 0) and (2 2 0) planes (Fig. 4B).

STEM images (Fig. 3) further prove the control of the formation of hexagonal platelet-like mosaics of NiO NCs. Dark-field STEM images confirmed the formation of porous NiO platelets with an average diameter of 250 nm and a thickness of less than 20 nm. STEM micrographs (insets) showed dense micro- and mesopore surface voids (open holes). In general, the formation of multidirectional porous NiO platelets with hexagonal mosaics may enhance the diffusion of pollutant molecules through the vicinity of the platelet mosaics during catalytic transformation.

3.3. Structural features of the NiO nanoplatelet-like mosaic catalysts

Fig. 4 shows the crystal structure of the as-made Ni(OH)$_2$ and the thermal-treated product of NiO powder, which were characterized via SAXS and wide angle X-ray diffraction (WAXRD). The SAXS profiles of the NiO platelets were subjected to absolute intensity
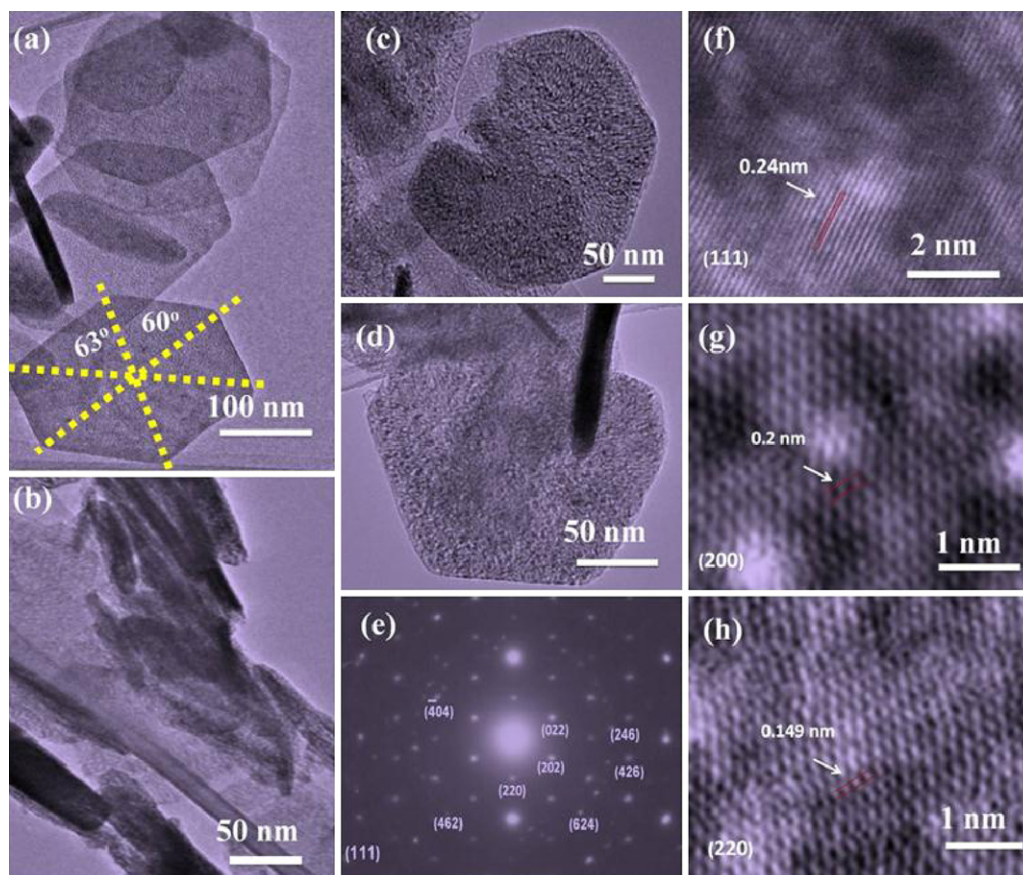
Fig. 2. Typical HRTEM images of multidirectional pores NiO nanoplatelets with an average size of 250 nm, nanoplatelet thickness of about 20 nm (a and b), magnified view of the acicular branch (c and d), and corresponding ED pattern of selected area (e). The HRTEM and ED patterns reveal the high crystallinity of the nanoplatelets.
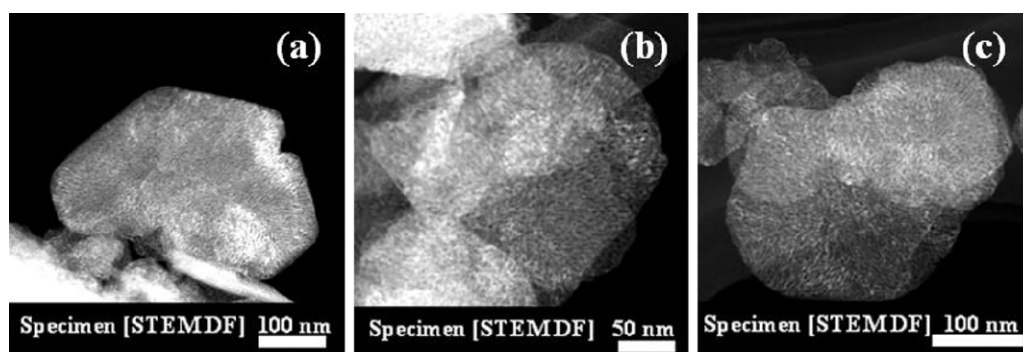

Fig. 3. STEM images of multidirectional pores NiO nanoplatelet-like mosaic with average size of 250 nm.
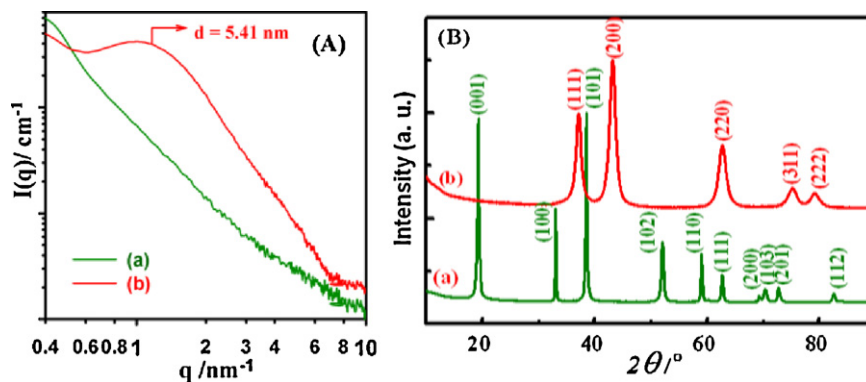

Fig. 4. (A) Small-angle X-ray scattering pattern, (B) wide-angle X-ray pattern of (a) the nickel oxide nanoplatelet and (b) hydrothermal product of $NiCl_2$ in pH 10, both indicating the formation of β-Ni(OH)$_2$ phase.
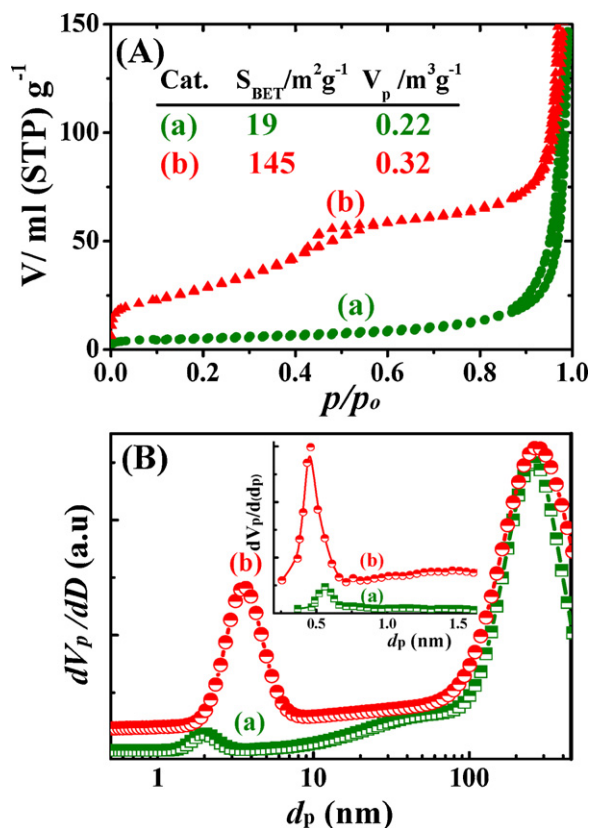
Fig. 5. (A) N_2 adsorption/desorption isotherms, (B) pore size distribution of (a) the Ni(OH)$_2$ nanoplatelet and (b) NiO nanoplatelets calculated using the NLDFT and HK methods.

scaling after in-plane diffracted beams with substrate thickness were normalized (Fig. 4A). The SAXS pattern of the Ni(OH)$_2$ sample did not show any scattering peaks (Fig. 4A(a)) because of amorphous pore networks within the Ni(OH)$_2$ nanoplatelets. After mild thermal treatment at 300 °C, Ni(OH)$_2$ decomposed to mesoporous NiO platelets (Fig. 4A(b)). The SAXS pattern of the NiO nanoplatelets showed a broadly resolved scattering peak at approximately $q = 1.16$ nm^{-1}, corresponding to $d_{spacing} = 5.41$ nm. Despite the broadening and low resolution in the intense scattering peak, the formation of mesostructures and retention of the mesopore architectures inside the NiO nanoplatelets were evident. This SAXS pattern (Fig. 4A(b)) is similar to the hexagonal mesoporous silica nanostrands fabricated using cationic surfactants as soft templates [38]. In conclusion, the boarding and low-resolution peaks indicated the formation of short-range order NiO mesostructures [39].

WAXRD patterns of the β-Ni(OH)$_2$ and NiO platelet-like mosaic are shown in Fig. 4(B). The WAXRD pattern of the hydrothermal product (Fig. 4B(a)) showed well-resolved and distinct diffraction peaks, indicating the formation of single-phase β-Ni(OH)$_2$ nanoplatelets with crystalline structures, consistent with JCPDS No. 14-0117, $a = 3.126$ Å. The WAXRD pattern of NiO (Fig. 4A(a)) showed typical strong diffraction peaks assigned to the (1 1 1), (2 0 0), (2 2 0), (3 1 1), and (2 2 2) planes with $d_{spacing} = 2.422$, 2.08, 1.48, 1.262, and 1.208 Å, respectively. These diffraction peaks coincided with the face-centered cubic Fm3m symmetry with a lattice constant of $a = 4.17$ Å (JCPDS No. 04-0835), as confirmed by the TEM profiles (Fig. 2e–h). Thus, the NiO NCs with platelet-like mosaics were produced from the conversion of β-Ni(OH)$_2$ to NiO during the dehydroxylation process under temperature treatment.

The textural properties of the NiO and β-Ni(OH)$_2$ nanoplatelets were further elucidated using N_2 isotherms (Fig. 5(A)). According to the IUPAC classification, the NiO nanoplatelets showed a

type IV isotherm with a small H2 hysteresis loop, indicating the formation of the mesoporous NiO [40]. The lower closure point of the hysteresis loop was observed in a very narrow range of relative pressures, which was approximately 0.42 or 0.52 for N_2 at 77 K, indicating the cavitation-induced stepwise desorption in the ink-bottle pores [41]. The desorption branch of the isotherms showed a stepwise behavior and ended at the limiting pressure of the hysteresis closure, implying non-uniformity of the pore openings associated with pore constrictions and/or ink-bottle pores with narrow necks. In turn, the N_2 isotherms of the as-made β-Ni(OH)$_2$ nanoplatelets showed type V isotherms, indicating the formation of micro/macropores. The high-pressure parts of the hysteresis loop ($0.9 < P/P_0 < 1$) may be associated with the textural larger pores that can be formed between the secondary platelet particles in the mosaic structures. The Ni(OH)$_2$ sample showed a low surface area and a low pore volume compared with the NiO nanoplatelets. The specific surface area was $S_{BET} = 19$ m^2 g^{-1} and 145 m^2 g^{-1} for Ni(OH)$_2$ and NiO-platelets, respectively. The Horvath–Kawazoe (HK) model was studied (Fig. 5B, insets) to investigate the microporosity of the platelet-like mosaics. The NiO platelets had multidirectional micro-, meso-, and macropores measuring 0.45, 3.6, and 270 nm, respectively (Fig. 5(B)). One of the main features of NiO nanoplatelets was the existence of micropores (4–6 Å) interconnecting the disordered mesopores [42], leading to a more suitable diffusion of the small molecules of the phenolic pollutants inside the entire micropore structure volumes ($V_m = 0.04$–0.06 cm^3/g). The NiO nanoplatelets had higher surface areas than those of the ordered mesoporous (108.6 m^2 g^{-1}) [43], as well as a microspherical structure [44] and a NiO flower-like morphology [45] that were recently fabricated through sophisticated methods.

3.4. Characteristics of the surface composition domains of NiO platelet catalysts

STEM-EDS mapping and X-ray photoelectron spectroscopy (XPS) analysis were performed to characterize the surface composition and atomic distribution of the NiO NCs. Fig. 6 shows the STEM-EDS mapping of the surface distribution of Ni, O, and C. The contribution of Ni and O was mainly in the formation of NiO NCs with hexagonal platelet-like mosaic; however, C was originally observed from the TEM grid. The STEM-EDS mapping indicated that Ni and O were uniformly distributed on the surface of the platelet. In addition, the intensity of Ni and O did not show co-incident regions of high or low intensity as would be expected if they occurred in a 1:1 atomic ratio of Ni:O as in NiO structures. Thus, significant differences in the atomic distribution of Ni and O were observed, as described in the XPS data. The elemental analysis of the NiO platelet using EDS (Fig. 6(b)) indicated the presence of Ni, O, C, and Pt. The existence of Pt and C peaks was attributed to the TEM grid. In addition, O and Ni were originally found in the NiO NCs, which had a [Ni]/[O] ratio of 0.77. The lower value compared with that of the stoichiometric NiO was because of the accession of the O atoms. Thus, the NiO nanoplatelet catalysts were composed of more O atoms and deficient in Ni atoms on the surface of the NiO, leading to intrinsic advantages in the catalytic transformation of organic species.

XPS technique was employed to elucidate the valence distribution and dispersion of the Ni ions in the NiO particles. The XPS patterns of the Ni2p spectra (Fig. 7a) showed two edges of 2p$_{1/2}$ (from about 869 eV to 885 eV) and 2p$_{3/2}$ (from about 850 eV to 867 eV). A Shirley background was applied across the Ni2p$_{3/2}$ portion of the spectra. The core level spectrum "edge" of the 3d transition metal composites was split into two signal peaks. The lowest energy peak at the ground state is called the main peak; however, the signal line at the excited final state is called the satellite peak [46]. The positions of the peaks were almost the same
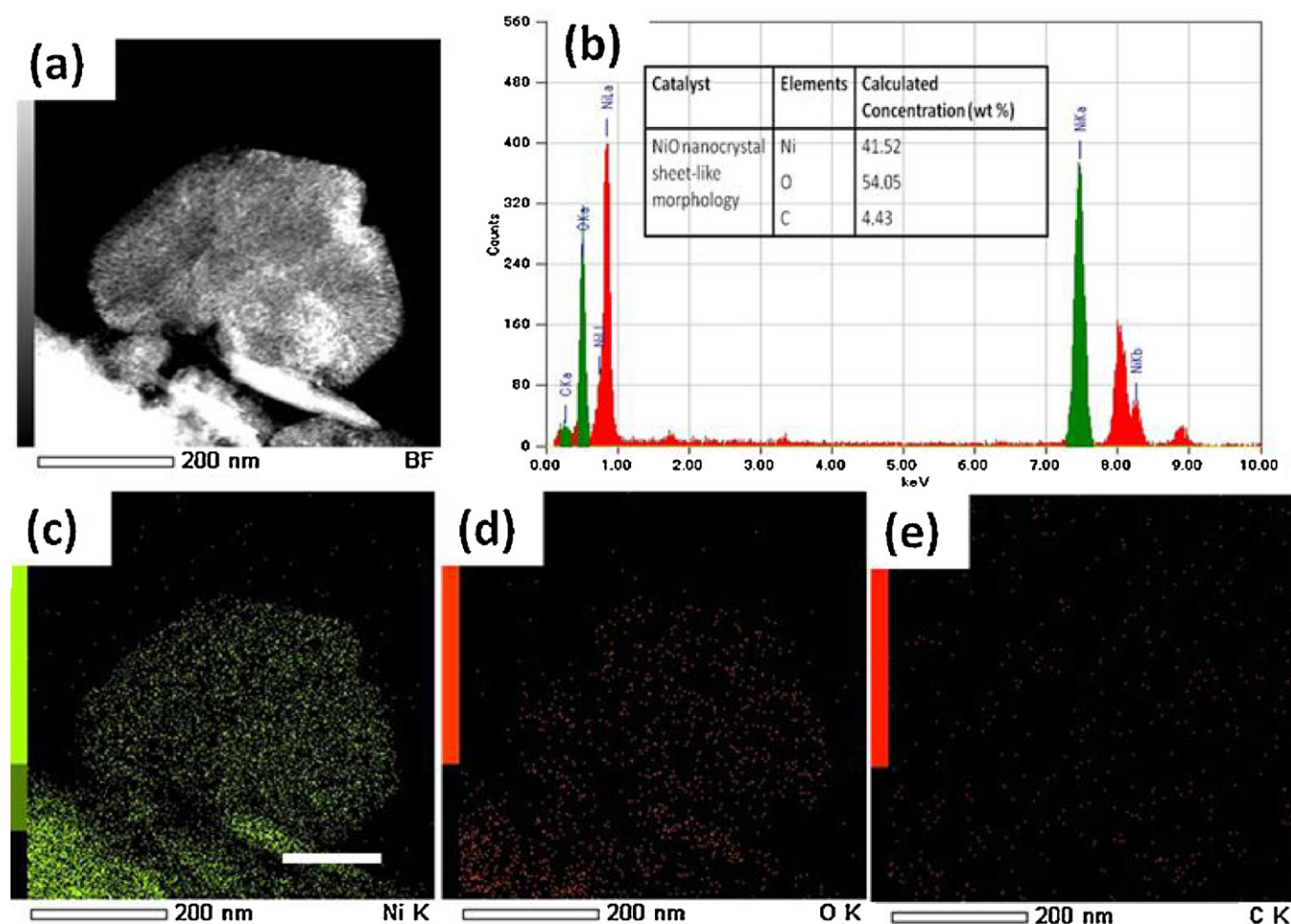
Fig. 6. STEM-EDS mapping, and EDS of the multidirectional pores NiO nanoplatelet; (a) STEM of NiO map, (b) EDS analysis, (c) nickel, (d) oxygen, and (e) carbon (inset) calculated values of atomic abundance of Ni and oxygen species present in the solid catalyst.
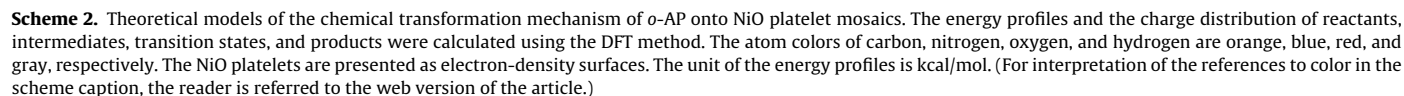
for $Ni(OH)_2$ and NiO within an experimental error. The $Ni2p_{1/2}$ (872 eV) and $Ni2p_{3/2}$ (853.2 eV) peaks were assigned to the Ni(II) ions in the NiO. The position of the peaks was close to the value of pure NiO (854.2 eV) with a slight shift to a lower binding energy. This shift in binding energy was attributed to the oxygen vacancy on the surface of the catalyst. The peak at 855 eV was ambiguous, which may be attributed to the Ni^{3+} species on the surface [47]. The splitting separation between these two main peaks, namely, 18.8 eV, indicated the well-defined symmetry of Ni(II) ions in oxide form. Fig. 7A shows two peaks of satellite structures at 860.5 and 864.6 eV. These satellite peaks may be assigned to the existence of the Ni(II) and Ni(III) ions; however, the latter was disregarded because of its low intensity and poor resolution compared with the Ni(II) satellite peak. The XPS results, in general, primarily indicated the dispersion of the dominant Ni(II) ions in intrinsic NiO particles. This finding indicated the contribution of NiO_6 in octahedral symmetry and NiO_5 in pyramidal symmetry containing more than one Ni ion in the core-hole sites. This result agreed with that in a previous report [48]. For the NiO nanoplatelets, many Ni and O atoms were found on the surface because of their porosity and nanosized nature, as shown in the STEM and STEM-EDS mapping (Figs. 3 and 6). Fig. 7b reveals the O1s XPS signal line with a distinct peak at 529.53 eV and a shoulder peak at 531.09 eV. The first peak was assigned to O bonded within a regular oxide crystal (O^{2-}). The second peak, which was a shoulder peak, could correspond to the defective sites within the NiO crystal assigned to O atoms in positions adjacent to Ni vacancies within the oxide

structure, adsorbed oxygen, or hydroxide species [49]. The surface atomic content of the NiO nanoplatelet was 40% for $Ni2p_{3/2}$, 48% for O1s, and 10% for C with an atomic ratio of about 0.84, indicating the oxygen overstoichiometry of NiO NCs on the surface [37–50].

3.5. Catalytic transformations of organic pollutants to hand-safe chemicals

3.5.1. Heterogeneous catalytic assay of porous NiO nanoplatelet catalysts

To investigate the catalytic performance of multidirectional micro-, meso-, and macroporous NiO nanoplatelet-like mosaics, o-AP and o-ATP were used as models for the transformation reactions (Fig. 8). The physical characteristics of NiO nanocatalyst, such as multidirectional porosity, surface area, and pore volume, enabled organic pollutants to access the active site of the nanoplatelet mosaics, leading to enhanced oxidation activity to form 3-aminophenoxazone (3-APZ) or 3-aminophenothiozine-3-thizone (3-APT) compounds, as shown in Scheme 2. Our finding reveals that the heterogeneous catalytic reaction depends on the temperature, solvent, and concentration of APs (Figs. 9 and 10, Fig. S3). Furthermore, the transformation reactions were performed in ethanol to study the effect of solvents on the catalytic rate (Fig. S3). The conversion rate of o-AP to 3-APZ in water was higher than the reaction in ethanol by about 1.8 times. This effect was a result of reactant solubility and their adsorption on the surface

Scheme 2. Theoretical models of the chemical transformation mechanism of o-AP onto NiO platelet mosaics. The energy profiles and the charge distribution of reactants, intermediates, transition states, and products were calculated using the DFT method. The atom colors of carbon, nitrogen, oxygen, and hydrogen are orange, blue, red, and gray, respectively. The NiO platelets are presented as electron-density surfaces. The unit of the energy profiles is kcal/mol. (For interpretation of the references to color in the scheme caption, the reader is referred to the web version of the article.)

of the catalyst, competitive adsorption of solvent, and interaction between the solvent and reactant molecules [51].

To demonstrate the applicability and efficiency of the hexagonal NiO platelet mosaic catalyst in these chemical transformation reactions, the heterogeneous catalytic reaction of o-AP was performed using a variety of NiO nanomaterials previously fabricated in nanoflower and nanoplatelet morphologies [43,44,52]. The results (Tables 1 to S9 and Fig. S4) revealed the higher catalytic efficiency of NiO platelet mosaics compared with NiO nanoflowers and nanoplatelets. Hence, textural surface parameters (S_{BET}, multidirectional pores, and pore volume), mosaic morphology, and surface composition played significant roles in the high-degree conversion of pollutants to hand-safe chemicals.

3.5.2. Physical studies of chemical transformation of phenolic pollutants

As shown in Fig. 9 and Table 1, the reaction was monitored at various temperatures (25–40 °C). K_c, and the negativity of ΔG increased with temperature. The purpose of the experiment was to investigate the kinetic and thermodynamic features of the transformation process of phenolic pollutants (o-AP and o-ATP) on the micro-, meso-, and macropore cavities of NiO platelet-like mosaics. Based on the results, the transformation reaction was spontaneous and more favorable at high temperatures, which confirmed an endothermic process with a positive value of ΔH. This finding indicated that the increase in reaction temperature facilitated the diffusion through the NiO pores. On the other hand, the

Table 1
Kinetic and thermodynamic features; heterogeneous reaction rate constant of the NiO nanocatalyst after recycling during oxidation of [0.5 mM] phenols at different temperatures.

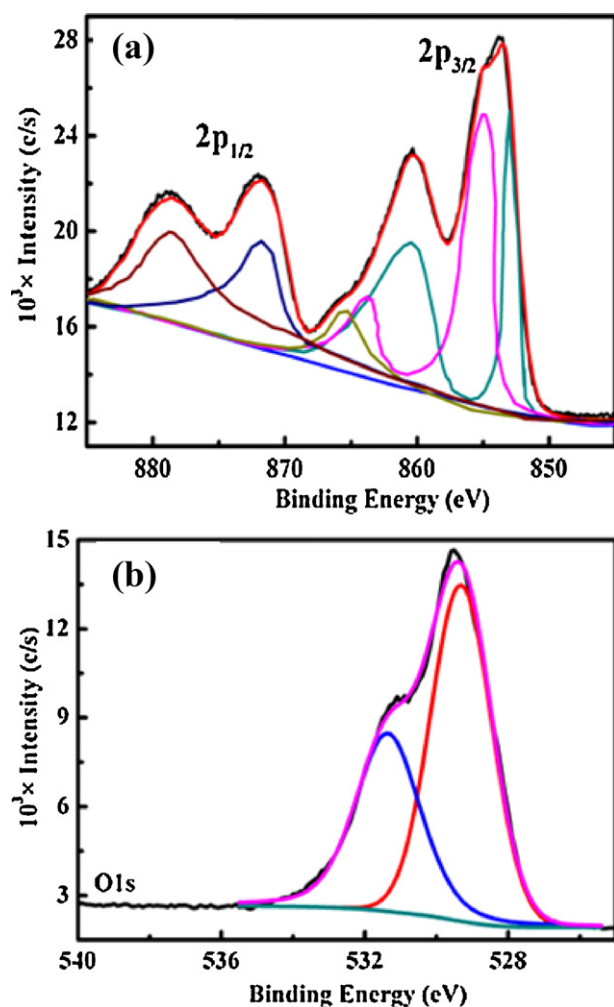| NiO nanoplatelet catalyst			Kinetic parameters					Thermodynamic parameters		
Pollutants	T (°C)	$10^3 \times$ (ks^{-1})	K_c	E_a (kJ mol^{-1})	$\Delta H^{\#}$ (kJ mol^{-1})	$\Delta S^{\#}$ (J mol^{-1} K^{-1})	$\Delta G^{\#}$ (kJ mol^{-1})	ΔH (kJ mol^{-1})	ΔS (J mol^{-1} K^{-1})	ΔG (kJ mol^{-1})
o-AP	25	9.50	0.69	28.88	26.31	−161.44	75.63	40.11	130.78	0.95
	30	11.37	0.76							0.70
	40	12.68	0.97							0.077
	45	17.05	1.51							−1.046
o-ATP	25	4.40	0.28	21.12	18.58	−193.67	77.75	44.86	139.79	3.23
	30	4.97	0.35							2.66
	40	5.75	0.50							1.76
	45	6.60	0.65							1.09

Fig. 7. XPS pattern of Ni2p (a) and O1s (b) spectra of NiO nanocatalyst synthesized via the hydrothermal method.
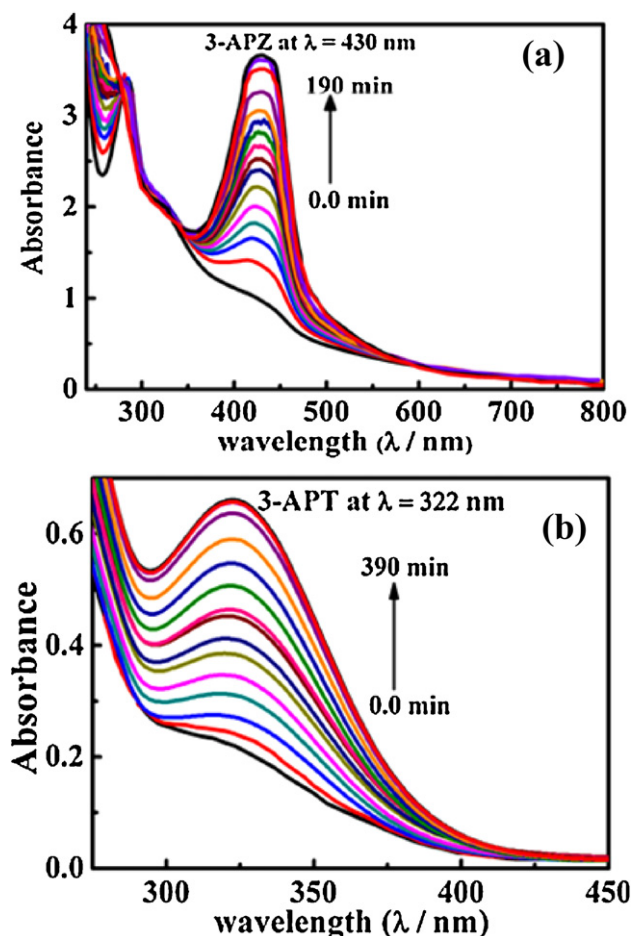

Fig. 8. UV–vis spectra of 3-APZ and 3-APT solutions in the course of catalytic reaction in the presence of NiO nanoplatelet {Reaction condition: 0.5 mM 3-APZ/3-APT in water, air atmosphere, NiO 0.83 g/L, and 25 °C}.
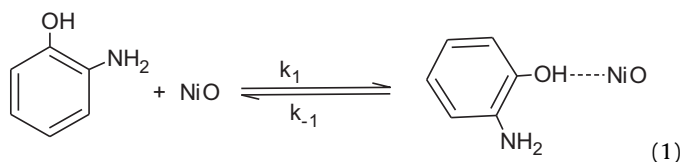
transformation reactions between the phenolic pollutants and a known amount of the NiO nanocatalyst followed first-order kinetics with respect to [phenol]. The first-order kinetics is as follows:

$$A_t = A_\infty \left(1 - \frac{1}{e^{kmt}}\right)$$

where A_∞ is the absorbance of 3-APZ or 3-APT at an infinite period of time; A_t is the absorbance of 3-APZ at time (t); k is the first-order rate constant (s^{-1}), which is only temperature dependent; and m (g) is the amount of NiO nanocatalyst in g (Figs. 10a and S5). The k of the heterogeneous catalytic reaction of the NiO nanoplatelets increased with increasing temperatures. The hexagonal nanoplatelet mosaics provided high accessibility, and the mobility of the small molecules of the phenolic pollutants, such as o-AP or o-ATP (about 6 Å), was crucially affected by the degree of porosity. The activation energy E_a of the phenolic pollutants was deduced from an Arrhenius plot ($k = Ae^{-E_a/RT}$, where k is the heterogeneous rate constant per gram of catalyst, R is the gas constant, and A is the frequency factor). The other activation parameters of the free energy of activation $\Delta G^{\#}$ (the enthalpy of activation $\Delta H^{\#}$ and the entropy of activation $\Delta S^{\#}$) were calculated using Eyring's equation ($k = (h/k_B T)e^{-\Delta G^{\#}/RT}$, where h is the Blank's constant and k_B is the Boltzmann constant) and are listed in Table 1. The $\Delta H^{\#}$ value of activation and the $\Delta G^{\#}$ value were in the range of the chemical reaction control. The transformation reactions were found to be entropy-controlled, as described in previous reports [53]. Furthermore, a greater $\Delta S^{\#}$

value of the chemical transformation of o-AP, compared with o-ATP, corresponded to the greater probability of activated complex formation, as shown in Table 1 and Scheme 2. The thermodynamic and kinetic parameters during the course of chemical transformation indicated the migration on pollutants through the interior of the micro-, meso-, and macropore cavities of NiO platelet mosaics [54].

3.5.3. Mechanistic studies of the chemical transformation of o-AP and o-ATP pollutants
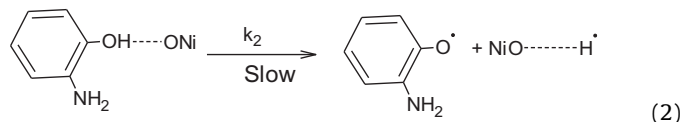
In general, the catalytic oxidation of phenol over the NiO nanocatalyst involved four electrons and four protons in producing 3-APZ and 3-APT, respectively (Scheme 2). For o-AP, benzo-imine was formed and then reacted with another molecule of o-AP to form dimeric oxidation products [55]. The reaction sequence of the expected oxidation products is shown in Scheme 2. Mass spectrometry was used to determine the molecular weight of the oxidation product of the transformation reaction of pollutants (Fig. S6). The results showed that the oxidation product of o-AP exhibited a molecular ion consistent with the formation of dimers [$C_{12}H_{11}N_2O_2$]. On the basis of the experimental results, two possibilities for the reaction of the o-AP molecules on the NiO nanocatalyst can be inferred. o-AP may have been present inside the pore or in the interlayer distance between the condensed platelets (Scheme 1). The textural surface parameters (surface area and pore volumes) with hexagonal nanoplatelet-like mosaics substantially influenced the catalytic functionality of the NiO surfaces. The heterogeneous catalytic transformation mechanism of the reaction

between phenol (P) and the metal oxide surface (NiO) occurred as shown in the mechanistic scheme.
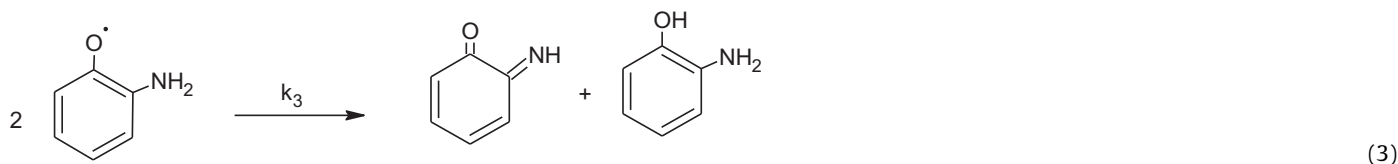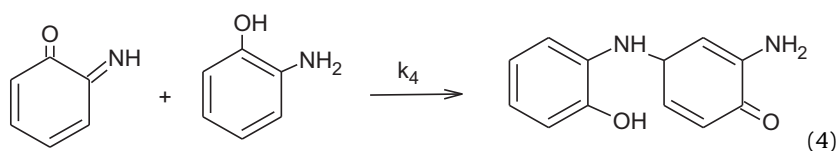
Surface physorption process
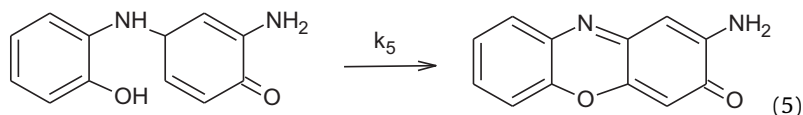

(1)

Formation of radical structure (TS1)

(2)

Formation of the metastable structure (IT)

(3)

Dimerization process of molecules

(4)

Cyclization process of dimer molecule

(5)

Note that the cyclization stages might consume two oxygen molecules for formation H_2O and reaction product. This particular formation stage can proceed on the surface of NiO catalyst. For the retention of the catalyst reactivity, the aqueous solution might regenerate the oxygen vacancy on the surface of the NiO catalyst.

The reaction rate;

$$-\frac{dx}{dt} = k_2 \, [\text{NiO}\cdots\text{P}] \tag{6}$$

Applying the steady-state approximation for the intermediate:

$$\frac{d\{[\text{NiO}\cdots\text{P}]\}}{dt} = k_1\{\text{NiO}\}[\text{P}] - k_{-1}[\text{NiO}\cdots\text{P}] - k_2\{\text{NiO}\cdots\text{P}^*\}] = 0 \tag{7}$$

where

$$[\text{NiO}\cdots\text{P}] = \frac{k_1\{\text{NiO}\}[\text{P}]}{k_{-1} + k_2} \tag{8}$$

$$-\frac{dx}{dt} = \frac{k_2 k_1 \{\text{NiO}\}\,[\text{P}]}{k_{-1} + k_2} \tag{9}$$

$$-\frac{dx}{dt} = k_{obs}\{\text{NiO}\}[\text{P}] \tag{10}$$

The experimental results suggested that the oxidation of phenolic pollutant via radical mechanism pathway. According to the kinetic data obtained and Eq. (10), the chemical transformation reaction rate is proportional to {NiO} and pollutant [P]. The reaction rate of phenol transformation followed first-order kinetics, which is consistent with that in previous studies [55], as shown in Figs. 10 and S5.

3.5.4. Theoretical models of the catalytic transformation reactions

The geometrical orientation of the functional groups −NH$_2$, −SH, and −OH is very important in heterogeneous catalytic transformation reactions. DFT calculations were performed for two reaction models using *o*-AP and *o*-ATP as reactants [36] to understand the proposed mechanism (Eqs. (1)–(5)). Scheme 2 shows the energy profiles of the oxidation reaction of pollutant [P] (e.g., *o*-AP molecule, and the charge distribution of the reactants, intermediates, transition states (TS), and products (S4)). The highest electronegative charge was attributed to the −NH$_2$ group (−0.57), suggesting that oxidation may have been induced by the electron loss from the −NH$_2$ group. One *o*-AP molecule was adsorbed on the nanoplatelet surface where the adsorption energy was about −15 kcal/mol. During the oxidation reaction, the first transition state (TS1) showed evidence of the formation of the *o*-AP radical

on the surface of the platelet [NiO$\cdots$*o*-AP$^\bullet$], as indicated in the proposed mechanism (TS1, Eq. (2)). The energy barrier for the produced radical structure (TS1) was about 38 kcal/mol. This highest energy level of the TS1 structure may have enabled the metastable outer-sphere orientation in the structure arrangement on the platelet surfaces {NiO$\cdots$*o*-AP} with a low energy of 5.8 kcal/mol intermediate (IT, Eq. (3)). The metastable structure led to the formation of the dimer throughout the combination to another *o*-AP molecule in the *p*-position with respect to the −OH group, which was the most electronegative part in the ring (−0.39) (TS2, Eq. (4)). The increase in the energy level (11.8 kcal/mole) of the TS2 dimer structure may be attributed to the rotation of the aromatic ring around the formed C-N bond to release the steric hindrance around the −OH group. Following the TS2 state formation, the cyclization step for the 3-APZ formation spontaneously occurred at the lowest energy level of −29 kcal/mol.

Furthermore, the cyclization reaction of *o*-ATP on the NiO platelet mosaics is presented in Fig. S9. The analysis of the orbital energies of the *o*-ATP and *o*-AP models showed the behavior of the intermediates for further cyclization (Tables 2 to S9). The electronic structure of the intermediates and products showed that the highest occupied molecular orbital-lowest unoccupied molecular orbital (HOMO–LUMO) band gap of both the *o*-ATP and *o*-AP molecules are very small. As the difference is insignificant, the phenol molecules may have the tendency for further polymerization.
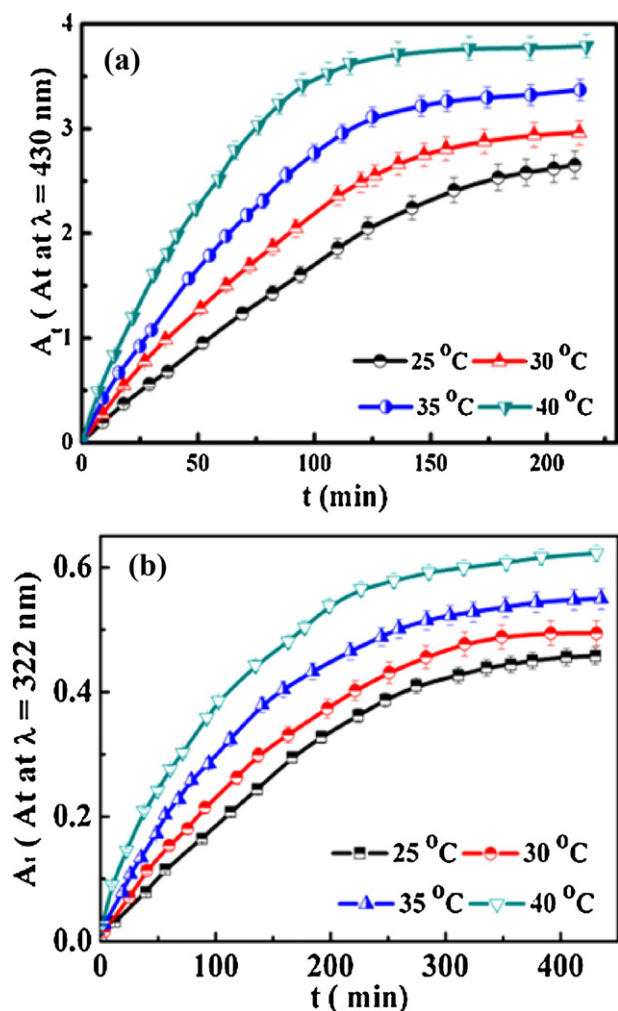
Fig. 9. Effect of various reaction temperatures on the time-rate dependence of the formation of 3-APZ at 430 nm (a) and 3-APT at 322 nm (b) during catalytic oxidation reactions of [0.5 mM] o-AP/o-ATP, respectively, over a NiO nanocatalyst.

3.5.5. Efficiency and reusability of NiO nanoplatelet catalysts

A major advantage of nanostructured catalysts is that they can maintain their activity toward the reaction media. Furthermore, the reusable catalyst should be safe, inexpensive, easy to handle
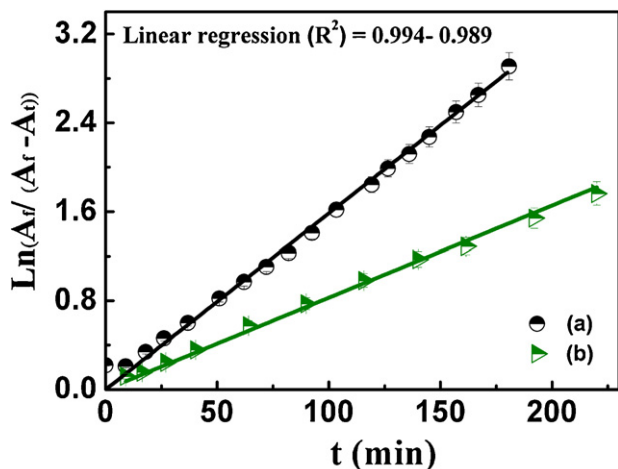

Fig. 10. Integrated first-order reaction rate of the catalytic transformation of [0.5 mM] o-AP (a) and o-ATP (b) over the NiO nanoplatelet.

Table 2
Catalytic reusability and phenol fractions covered with NiO nanocatalyst. The efficiency of the hexagonal NiO platelet mosaics was calculated from the % ratio of the coverage surface (f_c) of NiO mosaic catalysts per reuse cycle (No.) and the f_c obtained from the initial use of the catalysts.

Pollutants	$f_c \times 10^3$ (g m^{-2})	Catalyst reusability		
		Catalytic activity %		
		1st cycle	2nd cycle	4th cycle
o-AP	9.49	99.2	97.5	95
o-ATP	9.12	98.5	96	94.6

and dispose, and environmentally benign. Many of these methodologies suffer from the drawback of green chemistry and have been associated with several shortcomings, such as long reaction periods, expensive reagents, low product yields, and difficulty in catalyst recovery and reusability. Developing recyclable catalysts is important for industrial applications to solve these problems. After several regeneration/reuse cycles of the NiO catalysts, catalytic experiments showed no significant changes in the textural properties and catalytic efficiency of the oxidation of the phenol molecules (0.5 mM). The fractions of the coverage surface (f_c) occupied by the phenol molecules were calculated according to f_c (mg m^{-2}) = $M\beta/S$, where M is the molecular area of phenol molecules in the range of 60 Å^2 to 70 Å^2, S (m^2 g^{-1}) is the surface area of the catalyst, and β is the number of phenol molecules adsorbed per unit area of the catalyst. No significant changes in the affinity of the catalyst toward the chemical transformation reaction were observed after several cycles, as quantitatively evidenced by the coverage surface (f_c) of the NiO mosaic catalysts (Table 2).

Fig. 11 shows the catalytic efficiency of the NiO catalyst in each cycle. The NiO nanoplatelet catalysts lost about 5% of their original efficiency after six regenerations/reuse cycles without a change in structure or textural properties, as confirmed by the N$_2$ isotherms, SEM, and STEM profiles (Fig. S8). These findings indicated that the binding of organic moieties (reactant and product) onto the NiO catalyst does not lead to the deformation of the internal/external ordered and porous surface sites, despite the extended reuse cycles.
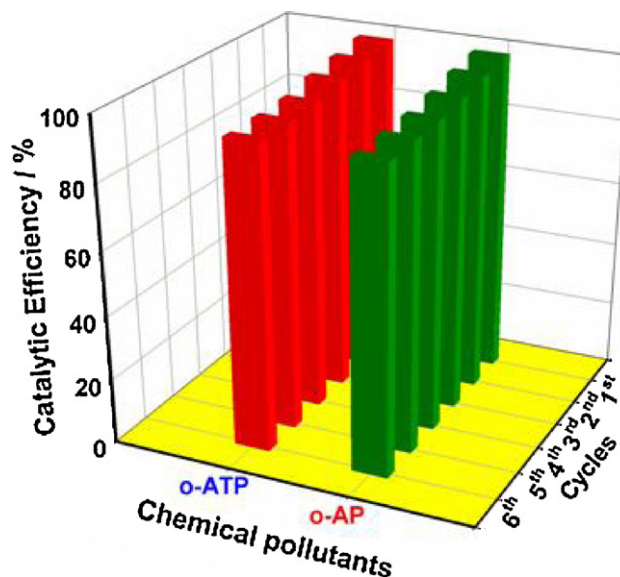

Fig. 11. Reproducibility and catalytic efficiency of the hexagonal NiO platelet mosaics after multiple cycles of heterogeneous catalytic transformation of [5 × 10^{-4} M] o-AP at 30 °C. The efficiency of the hexagonal NiO platelet mosaics (E) was calculated from the % ratio of the reaction rate constant (ks^{-1}) per reuse cycle (No.) and the initial reaction rate constant obtained from the initial use of the catalysts.

In general, NiO platelet mosaics showed better catalytic transformation of organic pollutants than mesoporous NiO-supported silica composites.

4. Conclusion

The morphology and chemical reactivity of hexagonal NiO nanoplatelet catalysts toward organic pollutants were investigated. The new approach features the fabrication of multidirectional micro-, meso-, and macroporous NiO NCs for large-scale production, low-cost manufacturing, and efficient transformation reaction. Moreover, the control of the size and shape of the NCs in condensed orientation "tesserae blocks" leads to the formation of hexagonal NiO platelet-like mosaics, which is also another aspect of the current approach. The platelet-like mosaic-enhanced accessibility and the interaction affinity of the phenolic pollutants for functional active sites of the NiO surfaces with Ni site deficiencies are intrinsic properties of NiO NCs. In addition, the multi-directional pores of the NiO catalyst were a key factor in the enhancement of the coverage surfaces and in the intra-particle diffusion on the network surfaces and into the pore architecture. Moreover, the transformation mechanism and dynamic orientation of the phenolic contaminants on the NiO surface are provided by a theoretical model (DFT). A key finding in the current study is that NiO NCs with platelet-like mosaics have excellent properties as catalysts for the chemical transformation of organic pollutants, and these NCs can retain their activity even after several reuse cycles. Such integration of NiO platelet catalysts is crucial to the further development of environmental cleanup catalysts for toxic organic molecules.

Appendix A. Supplementary data

Supplementary data associated with this article can be found, in the online version, at http://dx.doi.org/10.1016/j.apcatb.2012.04.021.

References

[1] T. Balaji, S.A. El-Safty, H. Matsunaga, T. Hanaoka, F. Mizukami, Angewandte Chemie International Edition 45 (2006) 7202.
[2] S.A. El-Safty, A.A. Ismail, H. Matsunaga, T. Hanaoka, F. Mizukami, Advanced Functional Materials 18 (2008) 1485.
[3] Y. Jin, C. Jia, S.W. Huang, M.O. Donnell, X. Gao, Nature Communications 1 (2010) 4.
[4] Y. Ren, P.G. Bruce, Z. Ma, Journal of Materials Chemistry 21 (2011) 9312;
   D.K. Kirui, D.A. Rey, C.A. Batt, Nanotechnology 21 (2010) 105.
[5] Y. Wang, A. Zhu, Y. Zhang, C.T. Au, X. Yang, Applied Catalysis B 81 (2008) 141–149.
[6] H.J. Gallon, X. Tu, M.V. Twigg, J.C. Whitehead, Applied Catalysis B 106 (2011) 616–620.
[7] S.A. El-Safty, A. Shahat, W. Warkocki, M. Ohnuma, Small 7 (2011) 62.
[8] S.A. El-Safty, Trends in Analytical Chemistry 30 (2011) 447.
[9] A. Chen, P. Holt-Hindle, Chemical Reviews 110 (2010) 3767.
[10] A.S. Zuruzi, N.C. MacDonald, M. Moskovits, A. Kolmakov, Angewandte Chemie International Edition 46 (4298) (2007).
[11] P. Yang, D. Zhao, D.I. Margolese, B.F. Chmelka, G.D. Stucky, Nature 396 (1998) 152.
[12] T.L. Lai, C.C. Lee, G.L. Huang, Y.Y. Shu, C.B. Wang, Applied Catalysis B: Environmental 78 (2008) 151.
[13] Y. Li, B.C. Zhang, X.W. Xie, J.L. Liu, Y.D. Xu, W.J. Shen, Journal of Catalysis 238 (2006) 412.
[14] P. Poizot, S. Laruelle, S. Grugeon, L. Dupont, J.M. Tarascon, Nature 407 (2000) 496.
[15] G. Mattei, P. Mazzoldi, M.L. Post, D. Buso, M. Guglielmi, A. Martucci, Advanced Materials 19 (2007) 561.
[16] A. Nattestad, M. Ferguson, R. Kerr, Y.B. Cheng, U. Bach, Nanotechnology 19 (2008) 295304.
[17] P. Jeevanandam, Y. Koltypin, A. Gedanken, Nano Letters 1 (2001) 263.
[18] N. Cordente, M. Respaud, F. Senocq, M.J. Casanove, C. Amiens, B. Chaudre, Nano Letters 1 (2001) 565.
[19] H. Liu, G. Wang, J. Liu, S. Qiao, H. Ahn, Journal of Materials Chemistry 21 (2011) 3046.
[20] N.M. Carneiro, W.C. Nunes, R.P. Borges, M. Godinho, L.E. Fernandez-Outon, W.A.A. Macedo, I.O. Mazali, Journal of Physical Chemistry C 114 (2010) 18773.
[21] D.B. Kuang, B.X. Lei, Y.P. Pan, X.Y. Yu, C.Y. Su, Journal of Physical Chemistry C 113 (2009) 5508.
[22] J. Hu, K. Zhu, L. Chen, H. Yang, Z. Li, A. Suchopar, R. Richards, Advanced Materials 20 (2008) 267.
[23] N.D. Hoa, S.A. El-Safty, Nanotechnology 22 (2011) 485503.
[24] T.-L. Lai, C.-C. Lee, K.-S. Wu, Y.-Y. Shu, Applied Catalysis B 68 (2006) 147–153;
   T.-L. Lai, C.-C. Lee, G.-L. Huang, Y.-Y. Shu, C.-B. Wang, Applied Catalysis B 78 (2008) 151–157.
[25] C.-B. Wang, Water for Life: Making it Happen, World Health Organization and UNICEF, 2005, ISBN 9241562935.
[26] C. Bradu, L. Frunza, N. Mihalche, S.-M. Avramescu, M. Neata, I. Udrea, Applied Catalysis B 96 (2010) 548–556.
[27] S.A. El-Safty, A. Shahat, M.R. Awual, Journal of Colloid and Interface Science 359 (2011) 9.
[28] A.A. Zagorodni, Ion Exchange Materials, Properties and Applications, Elsevier, Amsterdam, 2006.
[29] B.V. Bruggen, C. Vandecasteele, Environmental Pollution 122 (2003) 435.
[30] L.K. Posey, M.G. Viegas, A.J. Boucher, C. Wang, K.R. Stambaugh, M.M. Smith, B.G. Carpenter, B.L. Bridges, S.E. Baker, D.A. Perry, Journal of Physical Chemistry C 111 (2007) 12352.
[31] (a) U. Hollstien, Chemical Reviews 74 (1974) 625;
   (b) E. Frei, Cancer Chemotherapy Report 58 (1974) 49.
[32] C. Oishi, Bulletin of University Osaka Preference Series B 22 (1970) 49.
[33] P. Amrolia, S.G.A. Sullivan, S.R. Munday, Journal of Applied Toxicology 9 (1989) 113.
[34] Y.H. Hu, E. Ruckenstein, Langmuir 13 (1997) 2055;
   J. Li, R. Yan, B. Xiao, D.T. Liang, L. Du, Environmental Science & Technology 42 (2008) 6224.
[35] N.D. Hoa, S.A. El-Safty, Chemistry: A European Journal 17 (2011) 12896.
[36] M.J. Frisch, et al., Gaussian 03, Revision D.01, Gaussian, Inc., Wallingford, CT, 2004.
[37] Z.H. Liang, Y.J. Zhu, X.L. Hu, Journal of Physical Chemistry B 108 (2004) 3488.
[38] S.A. El-Safty, M. Mekawy, A. Yamaguchi, A. Shahat, K. Ogawa, N. Teramae, Chemical Communications 46 (2010) 3917.
[39] K.S. Napolskii, I.V. Roslyakov, A.A. Eliseev, A.V. Petukhov, D.V. Byelov, N.A. Grigoryeva, W.G. Bouwman, A.V. Lukashin, K.O. Kvashnina, A.P. Chumakov, S.V. Grigoriev, Journal of Applied Crystallography 43 (2010) 531.
[40] S.A. El-Safty, A. Shahat, M. Mekawy, H. Nguyen, W. Warkocki, M. Ohnuma, Nanotechnology 21 (2010) 603.
[41] M. Kruk, V. Antochshuk, J.R. Matos, L.P. Mercuri, M. Jaroniec, Journal of the American Chemical Society 124 (2002) 768.
[42] W.Q. Cai, J.G. Yu, B. Cheng, B.L. Su, M. Jaroniec, Journal of Physical Chemistry C 113 (2009) 14739.
[43] F. Jiao, A.H. Hill, A. Harrison, A. Berko, A.V. Chadwick, P.G. Bruce, Journal of the American Chemical Society 130 (2008) 5262.
[44] X. Song, L. Gao, Journal of Physical Chemistry C 112 (2008) 15299.
[45] B. Zhao, X.K. Ke, J.H. Bao, C.L. Wang, L. Dong, Y.W. Chen, H.L. Chen, Journal of Physical Chemistry C 113 (2009) 14440.
[46] Y. Hattori, Y. Konishi, K. Kaneko, Chemical Physics Letters 355 (2002) 37.
[47] M.J. Tomellini, Journal of Electron Spectroscopy and Related Phenomena 58 (1992) 75.
[48] M.C. Biesinger, B.P. Payne, W.M.L. Lau, A. Gerson, R.S.C. Smart, Surface and Interface Analysis 41 (2009) 324.
[49] (a) H.A.E. Hagelin-Weaver, J.F. Weaver, G.B. Hoflund, G.N. Salaita, Journal of Electron Spectroscopy and Related Phenomena 134 (2004) 139.
[50] R. Moreno-Tost, J. Santamaría-González, P. Maireles-Torres, E. Rodrguez-Castellón, A. Jiménez-López, Journal of Materials Chemistry 12 (2002) 3331.
[51] M.K. Moghaddam, A. Yangjeh, M. Reza Gholami, Journal of Molecular Catalysis A: Chemical 306 (2009) 11.
[52] X. Wang, L. Li, Y. Zhang, S. Wang, Z. Zhang, L. Fei, Y. Qian, Crystal Growth and Design 6 (2006) 9.
[53] A.B. Zaki, M.Y. El-Sheikh, J. Evans, S.A. El-Safty, Polyhedron 19 (2000) 1317.
[54] Y. Zhu, J. Li, Z. Liu, G. Cheng, S. Dong, E. Wang, Journal of Molecular Catalysis B: Enzymatic 4 (1998) 33.
[55] (a) J. Kaizer, R. Csonka, G. Speier, Journal of Molecular Catalysis A 180 (2002) 91;
   (b) S.A. El-Safty, Y. Kiyozumi, T. Hanaoka, F. Mizukami, Applied Catalysis A 337 (2008) 121–129.